ADVANCING EARTH AND SPACE SCIENCE

Geophysical Research Letters

RESEARCH LETTER
10.1029/2022GL102327

Using High-Resolution Satellite Imagery and Deep Learning to Track Dynamic Seasonality in Small Water Bodies

Andrew L. Mullen[1], Jennifer D. Watts[1], Brendan M. Rogers[1], Mark L. Carroll[2], Clayton D. Elder[3], Jonas Noomah[4], Zachary Williams[2,5], Jordan A. Caraballo-Vega[2], Allison Bredder[6], Eliza Rickenbaugh[7], Eric Levenson[8], Sarah W. Cooley[8], Jacqueline K. Y. Hung[1], Greg Fiske[1], Stefano Potter[1], Yili Yang[1], Charles E. Miller[3], Susan M. Natali[1], Thomas A. Douglas[9], and Ethan D. Kyzivat[10]

[1]Woodwell Climate Research Center, Falmouth, MA, USA, [2]NASA Goddard Space Flight Center, Greenbelt, MD, USA, [3]Jet Propulsion Laboratory, California Institute of Technology, Pasadena, CA, USA, [4]Northern Arizona University, Flagstaff, AZ, USA, [5]Now at Planet Labs Federal, Washington, DC, USA, [6]University of Maryland, College Park, MD, USA, [7]Montana State University, Bozeman, MT, USA, [8]University of Oregon, Eugene, OR, USA, [9]U.S. Army Cold Regions Research and Engineering Laboratory, Fort Wainwright, Fairbanks, AK, USA, [10]Brown University, Providence, RI, USA

Key Points:

- Deep learning and 3 m resolution satellite imagery from Planet Labs can detect and track ponds and lakes >0.0001 km^2
- Total surface area for ponds (<0.01 km^2) in boreal forest and tundra environments can vary by 20%–40% throughout an individual season
- Ponds can contribute to a broad range (8%–37%) of total methane emissions from lakes and ponds in northern boreal forest and tundra

Supporting Information:

Supporting Information may be found in the online version of this article.

Correspondence to:

A. L. Mullen,
amullen@woodwellclimate.org

Citation:

Mullen, A. L., Watts, J. D., Rogers, B. M., Carroll, M. L., Elder, C. D., Noomah, J., et al. (2023). Using high-resolution satellite imagery and deep learning to track dynamic seasonality in small water bodies. *Geophysical Research Letters*, *50*, e2022GL102327. https://doi.org/10.1029/2022GL102327

Received 29 NOV 2022
Accepted 6 MAR 2023

Abstract

Small water bodies (i.e., ponds; <0.01 km^2) play an important role in Earth System processes, including carbon cycling and emissions of methane. Detection and monitoring of ponds using satellite imagery has been extremely difficult and many water maps are biased toward lakes (>0.01 km^2). We leverage high-resolution (3 m) optical satellite imagery from Planet Labs and deep learning methods to map seasonal changes in pond and lake areal extent across four regions in Alaska. Our water maps indicate that changes in open water extent over the snow-free season are especially pronounced in ponds. To investigate potential impacts of seasonal changes in pond area on carbon emissions, we provide a case study of open water methane emission budgets using the new water maps. Our approach has widespread applications for water resources, habitat and land cover change assessments, wildlife management, risk assessments, and other biogeochemical modeling efforts.

Plain Language Summary

Small water bodies (<0.01 km^2) are an important driver of many Earth system processes. Despite their importance, many existing water mapping products have difficulty detecting these small water features and their seasonal changes in surface area. We used deep learning and high-resolution (3 m) satellite imagery to map and monitor seasonal changes in the areal extent of lakes and small ponds across four regions in Alaska. The resulting water maps accounted for considerably more water coverage than existing products. The maps also effectively tracked widespread seasonal changes in pond and lake area that were not previously identified. This demonstrates the importance of monitoring surface water at high spatial resolutions and across seasons.

1. Introduction

Lakes and ponds make up at least 3% of Earth's land surface (Downing, 2010; Downing et al., 2006; Messager et al., 2016; Verpoorter et al., 2014). These freshwater ecosystems support species diversity (Strayer & Dudgeon, 2010) and are sources of clean water for human populations (Ho & Goethals, 2019). They also play key roles in biogeochemical cycling and greenhouse gas emissions (Huotari et al., 2011; Kortelainen et al., 2020; Wik et al., 2016). In boreal and tundra regions, lakes and ponds comprise a much greater fraction (Muster et al., 2017; Verpoorter et al., 2014), exceeding 20% coverage in some areas (Arp et al., 2020; Carroll & Loboda, 2017; Cooley et al., 2019). High latitude lakes and ponds are heavily impacted by climate change (Webb et al., 2022; Xu et al., 2022), and many studies report severe changes in open water extent following shifts in precipitation patterns, loss of sub-surface permafrost, land collapse, and other climate-caused ecosystem disturbances (Arp et al., 2020; Bring et al., 2016; Finger-Higgens, 2022; Jones et al., 2011; Smith et al., 2005; Watts et al., 2014).

Surface area is a key attribute of water bodies and is related to their abundance, spatiotemporal variability, and methane (CH_4) emissions. Here we define ponds as water bodies <0.01 km^2 and lakes being >0.01 km^2, following the standard area threshold used in other studies (Holgerson & Raymond, 2016; Muster et al., 2017; Verpoorter et al., 2014). Ponds can be much more vulnerable to rapid change relative to lakes (Downing, 2010), yet they are often unaccounted for in existing surface water maps because of detection limits in remote sensing

imagery (Cooley et al., 2019; Wangchuk & Bolch, 2020). Many optical and active radar sensors used for water mapping do not have the requisite spatial or temporal resolutions to detect ponds and track the seasonality of their areal extent (Carroll & Loboda, 2017; DeVries et al., 2017; Du et al., 2019). Instead, past efforts have been biased toward lakes (Carroll & Loboda, 2017; DeVries et al., 2017; Pekel et al., 2016) and many water maps with high spatial resolutions are temporally static (Messager et al., 2016; Verpoorter et al., 2014). Undetected ponds introduce high uncertainty in estimations of CH_4, as ponds tend to be hotspots for CH_4 production (Negandhi et al., 2013; Wik et al., 2016). Since existing methods often fail to detect these small water features, CH_4 budgets likely underestimate emissions of this potent greenhouse gas (Walter Anthony et al., 2018).

The prevalence and importance of small water bodies call for novel mapping approaches that utilize advancements in very high-resolution remote sensing. The capacities of commercial satellite platforms have expanded considerably in recent years, providing new opportunities for monitoring water bodies. Maxar's Quickbird, WorldView-2 and -3 platforms offer unparalleled image clarity at resolutions <0.5 m, allowing delineation of fine water features (e.g., Kaiser et al., 2021; Setiawan et al., 2019). However, Maxar imagery can be unaffordable for regional applications and change analysis. Planet Labs' PlanetScope constellation (Planet Team, 2021) has over 200 optical satellites with 3–5 m resolutions, daily revisits, and more affordable pricing. PlanetScope has previously been used to track inundation extent (Cooley et al., 2019) and monitor the ecological variability of high latitude lakes (C. Kuhn et al., 2020, 2021). Research using PlanetScope to track lake shorelines found that open water mapping methods that rely on the normalized differenced water index (NDWI; McFeeters, 1996) ratios (i.e., higher pixel NDWI over water relative to dry ground) are unable to capture ponds in PlanetScope imagery (Cooley et al., 2019). An alternative water mapping method that used convolutional neural networks (CNN; i.e., deep learning) to detect lakes within the Himalaya using PlanetScope outperformed pixel-based approaches (Qayyum et al., 2020). However, the potential of PlanetScope imagery to track ponds remains unexplored.

This study leverages PlanetScope imagery to explore the feasibility of automated regional water body identification with CNNs, with the aim of detecting small ponds and seasonal changes in their extent. CNNs have proven effective in complex classification challenges, including detection of clouds (Caraballo-Vega et al., 2023; Kumthekar & Reddy, 2021), water flow paths (Stanislawski et al., 2021), and global real-time land-use/land-cover classification (Brown et al., 2022). We tested this approach using four case-study regions in Alaska and verified the water maps using on-ground Global Navigation Satellite System (GNSS) delineations. We then used monthly water body composite maps over the 3-year period to delineate areas having persistent open, standing water. Next, we investigated rapid surface water area variability by tracking individual water bodies throughout the 2021 snow-free season. Finally, we provided an example of how the new 3 m resolution water body maps compare to water maps from coarser-resolution satellite sensors, and a demonstration of how accounting for pond area greatly changes regional aquatic CH_4 budgets.

2. Materials and Methods

2.1. Study Areas

Our four study domains (i.e., areas of interest, AOI) were selected to span ecosystem gradients representative of boreal and tundra biomes in Alaska (Figure 1). Three AOIs are in Interior Alaska and represent complex boreal forest and wetland landscapes within a zone of discontinuous (50%–90%) permafrost (Pastick et al., 2015): Yukon Flats (YF; center coordinates: 66.509, −146.121; area: 9,440 km^2), Delta Junction (DJ; 63.826, −145.904; 7,110 km^2), and Fairbanks (FB; 64.793, −147.894; 6,200 km^2). DJ and FB cover terrains spanning headwaters within the Alaska Range to the low-lying Tanana River valley with numerous ponds and lakes. Both regions receive ~210 mm of precipitation during the snow-free season (May–September). The YF is a low-lying fluvial plain with highly dynamic rivers, streams, lakes, and ponds (Cooley et al., 2019; Nitze et al., 2018; Rey et al., 2019), receiving 115 mm of summer precipitation. The fourth AOI is located within the Yukon Delta National Wildlife Refuge, which is part of the Yukon-Kuskokwim Delta (YKD; 61.177, −163.232; 7,690 km^2). This region is characterized by peat plateau and wetland tundra overlying sporadic (10%–50%) to discontinuous permafrost (Pastick et al., 2015). The YKD receives 310 mm of summer precipitation and water coverage ranges from isolated water bodies to high-limnicity zones having >15% surface water (Nitze et al., 2018).

2.2. PlanetScope Imagery

We used Planet Labs PlanetScope orthotile surface reflectance imagery from the Dove-R and SuperDove sensors, provided through the NASA Commercial Smallsat Data Acquisition (CSDA) program. These two platforms

Figure 1. Delta Junction (DJ), Fairbanks (FB), Yukon Flats (YF), and Yukon-Kuskokwim Delta (YKD) case study regions. Shown are photographs of water bodies and the surrounding landscapes within each region.

provide daily coverage over the study regions from 2021 onward with less frequent coverage dating back to March 2019 (Roy et al., 2021). PlanetScope orthotiles are orthorectified, atmospherically corrected, and have a resolution of 3.125 m. The four-band imagery (blue, green, red, and near-infrared) overlaps closely with Sentinel-2 bands 2, 3, 4, and 8, allowing for testing and comparison of our deep learning method between PlanetScope and Sentinel-2. We used Planet's surface reflectance product to mitigate radiometric inconsistencies between scenes taken by different platforms at different viewing and solar zenith angles. Each PlanetScope orthotile has an accompanying "useable data mask" (UDM2) that flags pixels for snow, clouds, and haze (Planet Team, 2022).

2.3. Open Water Detection

This research focuses on detection of open, standing water, which we characterize as areas within lakes or ponds without obstruction from vegetation. We employ a deep learning approach (U-Net) to map open water as this approach considers spatial contextual information within the image and is likely less susceptible to uncertainties in the reflectance of individual pixels (Qayyum et al., 2020). Additional information on the U-Net approach and model development is provided in the Supporting Information S1 (Texts S1.1 and S1.2; Figures S1–S3).

The U-Net is a method of supervised classification, requiring training data. To train the U-Net (Text S1.3 in Supporting Information S1), we used PlanetScope orthotile imagery spanning a wide range of snow-free acquisition dates from the AOIs (Table S1 in Supporting Information S1 lists the training images). The training data set included 13,089 open water lakes and ponds that were hand-delineated in ArcGIS Pro v2.9 (ESRI, 2021), aided by 2 m Maxar WorldView-2/-3 imagery (Text S1.3 and Figure S2 in Supporting Information S1). We experimented with nine input data layers when training the U-Net. Input layers included PlanetScope red (R), green (G), blue (B), and near-infrared (NIR) surface reflectance bands. Additional candidate input layers included PlanetScope-derived: normalized difference vegetation index (NDVI); NDWI; saturation from the red, green, and blue channels (Sharma et al., 2015). NDVI, NDWI, and saturation layers were experimented with during initial model development, but were discarded from final model comparisons because they reduced accuracy scores considerably. To mitigate false-positive water detections in dark, terrain-shaded areas, we included layers

derived from the 30 m National Elevation Dataset (NED) digital elevation model (3DEP DEM; U.S. Geological Survey, 2020) which describe slope angle and topographic location. Text S1.4 in Supporting Information S1 contains details on the derived model input layers. For model training, 70% of the delineated water body data set was used for training, 20% was used for validation during model training, and 10% was withheld for testing after training. The U-Net model was deployed over PlanetScope Dove-R and SuperDove imagery with <10% cloud cover over the 2019–2021 snow-free period (Table S2 in Supporting Information S1). Raw U-Net predictions were post-processed (Text S1.5 in Supporting Information S1) to develop final water maps for each image.

2.4. Classification Accuracy Assessments

Model accuracy was assessed using two individual test sets. The U-Net was first tested on the 10% withheld data. We assessed the water body predictions using common accuracy metrics for image classification and segmentation including precision, recall, F1, and Intersection over Union (IOU; See Text S1.6 in Supporting Information S1 for more details). Briefly, precision quantifies the model's ability to correctly label open water, recall quantifies the model's ability to detect all open water, F1 takes the harmonic mean between precision and recall, and IOU calculates the spatial overlap between training water masks and U-Net predictions. For further verification we used GNSS surveys of open water ponds to examine the U-Net's accuracy. The GNSS delineations were obtained by walking shorelines of six open water bodies in DJ, 46 in the YKD, and one in Fairbanks. IOU scores were calculated using the GNSS shorelines and corresponding U-Net predictions from PlanetScope imagery captured within 1 week of the surveys. See Text S1.7 in Supporting Information S1; Figures S4 and S5 in Supporting Information S1 for a detailed description of this process.

2.5. Composite Water Maps

Cloud cover resulted in loss of quality image retrievals. To generate high-confidence water maps with complete data coverage over the AOIs, we composited U-Net predictions from images that spanned the 3 years of PlanetScope acquisitions (2019–2021). For each composite the occurrence ratio was calculated as the proportion of valid (cloud-free) observations where each pixel was detected as open water within a given time slice (Equation 1). Occurrence ratios ≥0.4 were given a value of 1 (open water), and occurrence ratios <0.4 were given a value of 0. This threshold was determined based on a visually optimal balance between false-positive (aggressive) and false-negative (conservative) predictions. 3-year composites were generated for each area using all available imagery from the snow-free periods. Monthly climatological composites were generated for DJ, FB, and YF AOIs for May–September using all imagery over the 3-year period for each given month. Monthly composites were not generated for the YKD due to lack of complete regional PlanetScope coverage for any given snow-free month. The monthly composites were averaged with the 3-year composites to further reduce geolocational error and anomalous predictions (Equation 2), which were more common in the raw monthly composites since they were generated with less overall predictions.

$$p_{\text{water}} = \frac{\#\,\text{water observations}}{\#\,\text{total valid observations}} \tag{1}$$

$$p_{\text{weighted}} = \frac{p_{\text{water}(3y)} + p_{\text{water(month)}}}{2} \tag{2}$$

2.6. Dynamic Water Tracking for 2021

The high cloud-free coverage provided by PlanetScope over each AOI in 2021 allowed us to effectively track individual water bodies over the May 24–September 19 period. First, individual water bodies were given unique identifiers by merging each monthly composite into a single map and adding a 30 m buffer around water bodies to avoid double-counting of single water bodies that were fragmented into multiple bodies by the model prediction (Cooley et al., 2019). This buffered mask represents the maximum extent of all water bodies present in the composite water maps, allowing for area tracking of individual water bodies. Water bodies with less than five observations throughout the 2021 growing season and individual predictions that were greater than the maximum buffered extent were removed from the time series. We smoothed individual water body time series using

a 7-observation median filter (Figure S6 in Supporting Information S1) to mitigate differences in area retrievals due to variability in lighting and atmospheric conditions, and geometric distortions between different image acquisitions. For each water body we quantified changes in surface area with the total (Equation 3) and fractional dynamism (Equation 4; Cooley et al., 2019), where a is the area for a water body on any given day.

$$\mathrm{dyn} = a_{\max} - a_{\min} \tag{3}$$

$$f_{\mathrm{dyn}} = \frac{a_{\max} - a_{\min}}{\sum_i a_{\max} - a_{\min}} \tag{4}$$

2.7. Product Comparisons

Water occurrence from the 3-year PlanetScope composites was compared with external water products derived from the Moderate Resolution Imaging Spectroradiometer (MODIS), Landsat, and Sentinel-2 satellite constellations to assess the advantages of high spatiotemporal resolution PlanetScope imagery. MOD44W v6 (MODIS-based, 250 m; Carroll et al., 2017) and the Joint Research Center's Surface Water Occurrence (JRC SWO; Landsat-based, 30 m; Pekel et al., 2016) surface water raster data were obtained using Google Earth Engine (Gorelick et al., 2017) for each AOI throughout the entire window of data collection for each respective product (2000–2015 for MOD44W and 1984–2020 for JRC SWO). Water in rivers was manually masked out of these products, and an occurrence ratio of 40% was used to threshold the MOD44W and JRC SWO maps. Text S2 in Supporting Information S1 contains details on the derivation of these products. A further step was to evaluate the Planet-derived maps against those derived from Sentinel-2. Given the spectral overlap of the PlanetScope blue, green, red, and near-infrared with Sentinel-2 bands 2, 3, 4, and 8, it was hypothesized that our U-Net approach might also be useful for detecting water within Sentinel-2 imagery. To test this hypothesis, we developed 3-year (2019–2021) Sentinel-2 composite water maps using the Planet-trained U-Net (See Text S2.3; Figure S7 in Supporting Information S1).

2.8. Water Map Application: Upscaling Methane Emissions

We used our resulting Planet-derived 3 m water maps to investigate the potential impact on high latitude CH_4 emission budgets, when accounting for ponds (also see Text S3 in Supporting Information S1). For this we used CH_4 fluxes from the Boreal-Arctic Wetland and Lake Methane Data set (BAWLD-CH_4; Kuhn, Varner, et al., 2021) to upscale emission estimates across each AOI. BAWLD-CH_4 reports median CH_4 emissions for different size classes of water bodies (small, medium, large) based on observations of CH_4 diffusion (1,134 lakes and ponds) and ebullition (202 lakes and ponds). We multiplied these median CH_4 emissions by the total area of each water body size class. In addition, we explored the co-location of spatial patterns observed between the 3 m water maps and >21,000 CH_4 hotspots in the YKD determined from hyperspectral Airborne Visible-Infrared Imaging Spectrometer - Next Generation (AVIRIS-NG) in an approach similar to Baskaran et al. (2022) and Elder et al. (2020, 2021).

3. Results and Discussion

3.1. Water Map Accuracy Assessments and Detection Limits

The U-Net approach detected ponds and lakes in our AOIs with high accuracy when using PlanetScope RGB NIR bands and 3DEP DEM-derived slope angle as inputs. Addition of the topographic layers (slope angle and TWI) had a negligible impact on accuracy scores, however, the slope layer greatly reduced false-positive detections over steeply sloping terrain based on visual assessment of the water maps. The trained U-Net had respective IOU, precision, recall and F1 scores of 0.91, 0.96, 0.95, and 0.95 (Text S1.8; Table S3 in Supporting Information S1). These scores are comparable to previous U-Net water body classifiers that used PlanetScope to map glacial lakes (Qayyum et al., 2020). Using the GNSS-based delineations (Text S1.7; Figure S5 in Supporting Information S1) the average IOU for ponds within the >0.001 km^2 and <0.01 km^2 size range was 0.81. Ponds within a smaller (>0.0001 km^2 and <0.001 km^2) size range had an average IOU of 0.40; 54% of these were at least partially detected. Based on this ground-surveyed data set we found the smallest detectable water body area

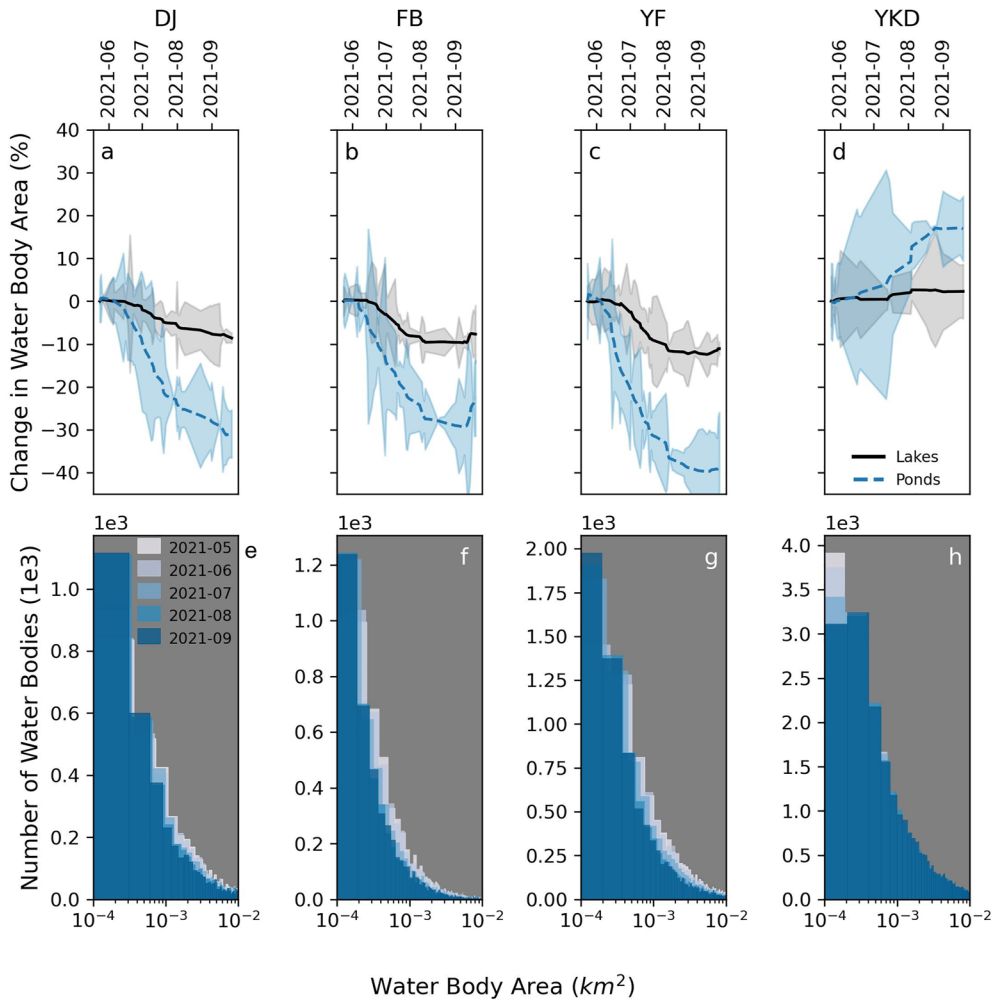

Figure 2. (a–d) Change in water body area as a percentage for each AOI. Solid black lines show the change in area for lakes (>0.01 km^2), and dashed blue lines show percent change in area for only ponds (<0.01 km^2). Shaded areas around the lines represent the root mean square error of the individual predictions around the filtered, interpolated area. (e–h) Histograms of water body size distributions averaged by month. Light gray is May, dark blue is for September 2021.

to be 0.0001 km^2 (Text S1.7; Figure S5 in Supporting Information S1), which is approximately equal to nine PlanetScope pixels. This size threshold is slightly higher than the minimum detectable water body size reported by studies using 2 m TerraSAR X radar (Muster et al., 2013) and <2 m Maxar optical imagery (Bouchard et al., 2014). Our method's detection limit is one order of magnitude finer than the Global Water Bodies Database (GLOWABO; Verpoorter et al., 2014) based on 15 m pan-sharpened Landsat imagery, and three orders of magnitude finer than the HydroLakes global lake data set (Messager et al., 2016).

3.2. Regional Surface Water Characteristics

The 3 m PlanetScope water maps allowed us to track ponds, in addition to lake areas, across the four AOIs (Figures S8a–S8l in Supporting Information S1, Movies S1–S4). Of the 52,797 water bodies present in the 3-year PlanetScope composite water maps, 77% were ponds, which had considerably higher percent dynamism than lakes over the 2021 snow-free period (Figure S9 in Supporting Information S1). Despite considerable seasonal changes in lake and pond surface area (Figures 2a–2d), monthly water body areas follow similar size distributions (Figures 2e–2h) found by previous studies (Kyzivat et al., 2019; Messager et al., 2016; Seekell & Pace, 2011; Verpoorter et al., 2014). Although size distributions did not change considerably across AOIs and months, the PlanetScope water body maps and area tracking highlight distinct differences in spatiotemporal water body characteristics between the four AOIs.

Lakes and ponds in DJ and FB had similar spatiotemporal characteristics due to the proximity of these two AOIs. The 3,481 detected ponds in DJ made up 21%–24% of the total lake and pond surface area in this AOI based on the monthly PlanetScope composites (Figures S10a and S10b in Supporting Information S1). Total pond surface area decreased by 31% in DJ during the 2021 snow-free season (Figure 2) which contributed to nearly half (43%) of total dynamism in water body surface area (Figures S10c and S10d in Supporting Information S1). DJ contained many stable lakes focused in lowland areas surrounding the Tanana River and its tributaries. Ponds had a greater contribution to total water body area and dynamism in FB due to their relative abundance, with a notable area south of the Tanana River where topography is extremely flat and the landscape is scattered with many small ponds that showed rapid decreases in surface area during summer. The monthly composite maps indicate that a total of 4,011 ponds in FB accounted for 26%–28% of total lake and pond surface area (Figures S10a and S10b in Supporting Information S1). The total surface area of ponds in FB decreased by 29% in 2021 (Figure 2), which represented 60% of the total dynamism in lake and pond surface area (Figures S10c and S10d in Supporting Information S1). Seasonal declines in lake and pond surface area in these AOIs contrasts with decadal-scale assessments that show increases in pond size and number due to melting permafrost (Walter Anthony et al., 2021). The dense time series imagery provided by PlanetScope can therefore be leveraged to decouple seasonal from climatological changes in water body characteristics.

In the YF, previous studies have found many large lakes with high dynamism (Cooley et al., 2019). It is hypothesized that this dynamism is potentially due to the connectivity of these lakes to groundwater beneath the permafrost (Rey et al., 2019), which is associated with increased hydraulic conductivity (Walvoord et al., 2012). The PlanetScope maps showed water bodies in YF to be larger on average (0.04 km^2) than DJ (0.01 km^2) and FB (0.006 km^2) (Figures S8g–S8i in Supporting Information S1). Given the abundance of lakes in YF it is unsurprising that the 6,626 ponds made up only 5% of total water body area in this AOI (Figures S10a and S10b in Supporting Information S1). Ponds experienced a 40% decrease in total surface area during 2021 (Figure 2) which represented 22% of the total dynamism in water body surface area (Figures S10c and S10d in Supporting Information S1). In YF, ponds contributed less to total surface water variability than DJ and FB due to the large number of lakes with high percent dynamism (Figure S9 in Supporting Information S1).

Water body coverage was much more spatially heterogeneous in the tundra landscape of the YKD, ranging from zones of isolated ponds in the center of the AOI, zones of high limnicity with large, densely packed lakes in the south, and a small area in the northwest of the AOI with little to no water bodies (Figure S8j in Supporting Information S1). The YKD had a much higher percentage of open water bodies (27.9%) than the boreal AOIs (DJ: 0.6%, FB: 0.4%, YF: 4%) and water bodies were larger on average (0.06 km^2). A total of 26,624 ponds detected in the YKD made up 5% of the total water body area in the YKD (Figures S10a and S10b in Supporting Information S1). Similar to the boreal AOIs, the variability of pond surface area clearly outsized the contribution of ponds to total water body area. However, surface area increased for both lakes (2%) and ponds (18%) in the YKD in 2021 (Figure 2), and ponds contributed to 10% of total water body surface area variability (Figures S10c and S10d in Supporting Information S1). During July 2021, the YKD experienced the greatest amount of precipitation for July on record since the 1920s (NOAA National Centers for Environmental Information, 2021), indicating that the observed variability in water body surface area in the YKD could be rainfall driven. This variability contrasts with the boreal regions which showed characteristics of snowmelt-driven change. In addition to rainfall, permafrost thaw in the YKD could also have impacted surface water area over the 2021 summer (Grosse et al., 2013). The seasonality of water body surface area in the YKD is poorly characterized in previous research, however, studies have found late-season increases in lake area in the Mackenzie River Delta (Cooley et al., 2019) and water area increases across multi-year timescales in Arctic deltas (Carroll & Loboda, 2017; Nitze et al., 2018).

3.3. Evaluation Against Other Surface Water Products

The PlanetScope water body maps provided insights into the importance of capturing ponds for evaluation of seasonal water body characteristics. We compared the PlanetScope water body maps with water maps from coarser-resolution remote sensing imagery to investigate the advantages of the high-resolution commercial imagery (Figures S8a–S8l in Supporting Information S1). Statistics from the comparisons are summarized in Table S4 and Figures S11a–S11d in Supporting Information S1.

Over the four AOIs, the 3 m PlanetScope water maps detected 8% more total water body surface area than the 10 m Sentinel-2 product, 18% more surface area than the 30 m JRC SWO (Pekel et al., 2016), and 22% more surface area than the 250 m MOD44W (Carroll et al., 2017). Discrepancies between the PlanetScope water maps

and the coarser-resolution products were almost entirely based on water body surface area relative to the spatial resolution of each product. IOU scores between each respective product and the PlanetScope maps diminished with decreasing water body surface area (Figure S11a in Supporting Information S1), approaching zero at different area thresholds for each product (Figures S11c and S11d in Supporting Information S1). MOD44W failed to detect 44,000 water bodies, as the 250 m MODIS pixels largely limit detection to water bodies >0.1 km^2. 38,000 water bodies present in the PlanetScope water maps were missing from the JRC SWO product, which is likely due to the difficulty in resolving water bodies <0.01 km^2 with the 30 m Landsat resolution. The 10 m Sentinel-2 product captured water bodies as small as 0.001 km^2, but this lower limit still resulted in 23,000 missed water bodies that were present in the PlanetScope water maps.

Temporal differences between the water body products led to disagreement in the YKD, where the coarser-resolution products failed to detect many larger water bodies (Figure S11d in Supporting Information S1). Inspection of the PlanetScope 3-year composite water body maps and PlanetScope imagery indicates that many of these water bodies were only present for brief periods of time after snowmelt (Late May). Since cloud-free observation windows are sparse over the YKD, the absence of these rapidly diminishing water bodies in the three external products was likely due to their relatively coarse temporal resolutions with respect to PlanetScope.

In terms of total water body area, differences in water detection capabilities between PlanetScope and the highest-resolution product that was compared (Sentinel-2; 10 m) seem minimal when considering the costs of commercial satellite data. However, PlanetScope's advantage clearly lies in its ability to detect small ponds >0.0001 km^2, which resulted in 77% more water bodies represented in the PlanetScope maps than in the Sentinel-2 maps. Additionally, the daily revisit of PlanetScope provides five times the amount of observations as the Sentinel-2a -2b constellation (5-day revisit), allowing for more observations within cloud-free windows that are sparse in many regions of the globe.

3.4. Tracking CH_4 Emissions From Open Water and CH_4 Hotspot Occurrence

CH_4 from ponds has largely been excluded from regional CH_4 budget studies due to the difficulty in detecting ponds using coarser-resolution water body datasets. Through spatial upscaling of aquatic flux rates based on the BAWLD-CH_4 synthesis (C. Kuhn, John, et al., 2021) and our new 3 m PlanetScope open water maps, we estimated that ponds and lakes contributed to 0.39 (DJ), 0.35 (FB), 1.57 (YF), and 6.26 (YKD) mg CH_4 per day per m^2 of each respective AOI. Considering the temporal variability in pond extent based on the monthly PlanetScope composites, ponds alone contributed to 24%–28% of upscaled aquatic CH_4 emissions in DJ, 30%–37% in FB, 8%–10% in YF, and 15% in the study portion of the YKD (Figure S12 in Supporting Information S1). The observed temporal variability in CH_4 emissions from lakes and ponds is conservative compared to PlanetScope-based estimates from the mid-latitudes (Hondula et al., 2021), which could be due to environmental factors or the relatively coarse temporal resolution of our monthly composite water maps. Additionally, comparison of the AVIRIS-NG-derived CH_4 hotspot maps to the 3-year PlanetScope composite revealed that CH_4 hotspot occurrences were three times higher around ponds (177 hotspots per km^2) than lakes in the study portion of the YKD (54 hotspots per km^2) (Text S3.2, Figure S13 in Supporting Information S1). Given the detection limits of the coarser-resolution surface water products investigated in this study, the contribution of ponds to total upscaled aquatic CH_4 emissions would not be quantifiable with Landsat and MODIS-based surface water products. Although Sentinel-2 showed the ability to detect ponds, total upscaled CH_4 emissions from ponds were still 28% lower over the snow-free season when using the Sentinel-2 product as opposed to PlanetScope (Figure S12 in Supporting Information S1), due to the ability of PlanetScope to capture ponds an order of magnitude smaller than Sentinel-2.

Area alone is not always a good predictor of CH_4 emissions from water bodies (Kohnert et al., 2018; Rehder et al., 2021), the emission data set used in our upscaling is not necessarily representative of aquatic CH_4 emissions in our AOIs, and the PlanetScope water maps generated in this study do not identify wet vegetated areas that tend to produce higher CH_4 emissions (Kyzivat et al., 2022; Villa et al., 2021). However this example presents the first critical steps in incorporating the effects of ponds and their seasonality on regional aquatic CH_4 emissions and CH_4 hotspot occurrence.

4. Conclusions

High spatiotemporal resolution satellite imagery from Planet Labs and deep learning provide new and improved means for detecting and tracking very small water bodies over time. These water maps have applications across

many disciplines that require monitoring rapid changes in surface water extent, and modeling applications where small water bodies have a considerable influence on the relevant process (e.g., CH_4 emissions). There are undoubtedly ponds <0.0001 km^2 that our PlanetScope imagery is unable to resolve. While these small water bodies may not contribute significantly to total surface water area and variability, they likely have a much greater influence on the total number of water bodies and CH_4 emissions. With ever-improving capabilities of commercial optical and new radar satellite platforms (e.g., Capella Space X-band synthetic aperture radar), the capacity for high spatiotemporal resolution monitoring of surface water is greater than ever. We present an approach that leverages these new capabilities to enhance our understanding of fine-scale land surface changes that have broad-scale implications.

Data Availability Statement

The 3-year and monthly climatological PlanetScope lake and ponds maps generated for this research can be accessed at https://doi.org/10.3334/ORNLDAAC/2134 (Mullen et al., 2022). Code supporting the findings from this research is available at https://doi.org/10.5281/zenodo.7689695 (Mullen, 2023a). U-Net model files (.h5 format) are available at https://doi.org/10.5281/zenodo.7682754 (Mullen, 2023b).

Acknowledgments
This research was primarily funded through a 2020 NASA ABoVE CSDA Grant (80NSSC21K1161). We also acknowledge support from the Gordan and Betty Moore Foundation (8414) and the Woodwell Fund for Climate Solutions. S. Cooley and E. Levenson were funded by NASA Grant 80NSSC21K0920. T. Douglas acknowledges funding from the U.S. Army Corps of Engineers Engineer Research and Development Center Applied Research Program Office for Installations and Operational Environment and Basic Research Program under PE 0601102/AB2 (Protection, Maneuver, Geospatial, Natural Sciences). Components of this research were carried out at the Jet Propulsion Laboratory, California Institute of Technology, under a contract with the National Aeronautics and Space Administration (80NM0018D0004). Computing resources were provided through the NASA High-End Computing (HEC) Program through the NASA Center for Climate Simulation (NCCS) at Goddard Space Flight Center. This work also utilized synthetic-aperture radar imagery courtesy of Capella Space's Data Grant Program, (c) 2022, All Rights Reserved. Authors also acknowledge Valeria Briones (Woodwell Climate Research Center) for fieldwork assistance.

References

Arp, C. D., Whitman, M. S., Kemnitz, R., & Stuefer, S. L. (2020). Evidence of hydrological intensification and regime change from northern Alaskan watershed runoff. *Geophysical Research Letters*, *47*(17), e2020GL089186. https://doi.org/10.1029/2020GL089186

Baskaran, L., Elder, C., Bloom, A. A., Ma, S., Thompson, D., & Miller, C. E. (2022). Geomorphological patterns of remotely sensed methane hot spots in the Mackenzie Delta, Canada. *Environmental Research Letters*, *17*(1), 015009. https://doi.org/10.1088/1748-9326/ac41fb

Bouchard, F., Francus, P., Pienitz, R., Laurion, I., & Feyte, S. (2014). Subarctic thermokarst ponds: Investigating recent landscape evolution and sediment dynamics in thawed permafrost of northern Québec (Canada). *Arctic Antarctic and Alpine Research*, *46*(1), 251–271. https://doi.org/10.1657/1938-4246-46.1.251

Bring, A., Fedorova, I., Dibike, Y., Hinzman, L., Mård, J., Mernild, S. H., et al. (2016). Arctic terrestrial hydrology: A synthesis of processes, regional effects, and research challenges. *Journal of Geophysical Research: Biogeosciences*, *121*(3), 621–649. https://doi.org/10.1002/2015JG003131

Brown, C. F., Brumby, S. P., Guzder-Williams, B., Birch, T., Hyde, S. B., Mazzariello, J., et al. (2022). Dynamic world, near real-time global 10 m land use land cover mapping. *Scientific Data*, *9*(1), 251. https://doi.org/10.1038/s41597-022-01307-4

Caraballo-Vega, J. A., Carroll, M. L., Neigh, C. S. R., Wooten, M., Lee, B., Weis, A., et al. (2023). Optimizing WorldView-2, -3 cloud masking using machine learning approaches. *Remote Sensing of Environment*, *284*, 113332. https://doi.org/10.1016/j.rse.2022.113332

Carroll, M., DiMiceli, C., Wooten, M., Hubbard, A., Sohlberg, R., & Townshend, J. (2017). MOD44W MODIS/terra land water mask derived from MODIS and SRTM L3 global 250m SIN grid V006. [Dataset]. NASA EOSDIS Land Processes DAAChttps://doi.org/10.5067/MODIS/MOD44W.006

Carroll, M., & Loboda, T. (2017). Multi-decadal surface water dynamics in North American Tundra. *Remote Sensing*, *9*(5), 497. https://doi.org/10.3390/rs9050497

Cooley, S. W., Smith, L. C., Ryan, J. C., Pitcher, L. H., & Pavelsky, T. M. (2019). Arctic-boreal lake dynamics revealed using CubeSat imagery. *Geophysical Research Letters*, *46*(4), 2111–2120. https://doi.org/10.1029/2018GL081584

DeVries, B., Huang, C., Lang, M., Jones, J., Huang, W., Creed, I., & Carroll, M. (2017). Automated quantification of surface water inundation in wetlands using optical satellite imagery. *Remote Sensing*, *9*(8), 807. https://doi.org/10.3390/rs9080807

Downing, J. A. (2010). Emerging global role of small lakes and ponds: Little things mean a lot. *Limnética*, *29*(1), 9–24. https://doi.org/10.23818/limn.29.02

Downing, J. A., Prairie, Y. T., Cole, J. J., Duarte, C. M., Tranvik, L. J., Striegl, R. G., et al. (2006). The global abundance and size distribution of lakes, ponds, and impoundments. *Limnology & Oceanography*, *51*(5), 2388–2397. https://doi.org/10.4319/lo.2006.51.5.2388

Du, J., Watts, J. D., Jiang, L., Lu, H., Cheng, X., Duguay, C., et al. (2019). Remote sensing of environmental changes in cold regions: Methods, achievements and challenges. *Remote Sensing*, *11*(16), 1952. https://doi.org/10.3390/rs11161952

Elder, C. D., Thompson, D. R., Thorpe, A. K., Chandanpurkar, H. A., Hanke, P. J., Hasson, N., et al. (2021). Characterizing methane emission hotspots from thawing permafrost. *Global Biogeochemical Cycles*, *35*(12), e2020GB006922. https://doi.org/10.1029/2020GB006922

Elder, C. D., Thompson, D. R., Thorpe, A. K., Hanke, P., Walter Anthony, K. M., & Miller, C. E. (2020). Airborne mapping reveals emergent power law of Arctic methane emissions. *Geophysical Research Letters*, *47*(3), e2019GL085707. https://doi.org/10.1029/2019GL085707

Esri Inc. (2021). *ArcGIS Pro (version 2.9)*. Esri Inc. Retrieved from https://www.esri.com/en-us/arcgis/products/arcgis-pro/overview

Finger-Higgens, R. (2022). Diminishing Arctic lakes. *Nature Climate Change*, *12*(9), 782–783. https://doi.org/10.1038/s41558-022-01466-7

Gorelick, N., Hancher, M., Dixon, M., Ilyushchenko, S., Thau, D., & Moore, R. (2017). Google Earth engine: Planetary-scale geospatial analysis for everyone. *Remote Sensing of Environment*, *202*, 18–27. https://doi.org/10.1016/j.rse.2017.06.031

Grosse, G., Jones, B., & Arp, C. (2013). 8.21 Thermokarst lakes, drainage, and drained basins. In *Treatise on geomorphology* (pp. 325–353). Elsevier. https://doi.org/10.1016/B978-0-12-374739-6.00216-5

Ho, L. T., & Goethals, P. L. M. (2019). Opportunities and challenges for the sustainability of lakes and reservoirs in relation to the sustainable development goals (SDGs). *Water*, *11*(7), 1462. https://doi.org/10.3390/w11071462

Holgerson, M. A., & Raymond, P. A. (2016). Large contribution to inland water CO_2 and CH_4 emissions from very small ponds. *Nature Geoscience*, *9*(3), 222–226. https://doi.org/10.1038/ngeo2654

Hondula, K. L., DeVries, B., Jones, C. N., & Palmer, M. A. (2021). Effects of using high resolution satellite-based inundation time series to estimate methane fluxes from forested wetlands. *Geophysical Research Letters*, *48*(6), e2021GL092556. https://doi.org/10.1029/2021GL092556

Huotari, J., Ojala, A., Peltomaa, E., Nordbo, A., Launiainen, S., Pumpanen, J., et al. (2011). Long-term direct CO_2 flux measurements over a Boreal lake: Five years of eddy covariance data: CO_2 fluxes of a Boreal lake. *Geophysical Research Letters*, *38*(18), L18401. https://doi.org/10.1029/2011GL048753

Jones, B. M., Grosse, G., Arp, C. D., Jones, M. C., Walter Anthony, K. M., & Romanovsky, V. E. (2011). Modern thermokarst lake dynamics in the continuous permafrost zone, northern Seward Peninsula, Alaska. *Journal of Geophysical Research*, *116*, G00M03. https://doi.org/10.1029/2011JG001666

Kaiser, S., Grosse, G., Boike, J., & Langer, M. (2021). Monitoring the transformation of Arctic landscapes: Automated shoreline change detection of lakes using very high resolution imagery. *Remote Sensing*, *13*(14), 2802. https://doi.org/10.3390/rs13142802

Kohnert, K., Juhls, B., Muster, S., Antonova, S., Serafimovich, A., Metzger, S., et al. (2018). Toward understanding the contribution of waterbodies to the methane emissions of a permafrost landscape on a regional scale—A case study from the Mackenzie delta, Canada. *Global Change Biology*, *24*(9), 3976–3989. https://doi.org/10.1111/gcb.14289

Kortelainen, P., Larmola, T., Rantakari, M., Juutinen, S., Alm, J., & Martikainen, P. J. (2020). Lakes as nitrous oxide sources in the boreal landscape. *Global Change Biology*, *26*(3), 1432–1445. https://doi.org/10.1111/gcb.14928

Kuhn, C., Bogard, M., Johnston, S. E., John, A., Vermote, E., Spencer, R., et al. (2020). Satellite and airborne remote sensing of gross primary productivity in boreal Alaskan lakes. *Environmental Research Letters*, *15*(10), 105001. https://doi.org/10.1088/1748-9326/aba46f

Kuhn, C., John, A., Hille Ris Lambers, J., Butman, D., & Tan, A. (2021). Arctic-Boreal Lake phenology shows a relationship between earlier lake ice-out and later green-up. *Remote Sensing*, *13*(13), 2533. https://doi.org/10.3390/rs13132533

Kuhn, M. A., Varner, R. K., Bastviken, D., Crill, P., MacIntyre, S., Turetsky, M., et al. (2021). BAWLD-CH_4: A comprehensive dataset of methane fluxes from boreal and arctic ecosystems. *Earth System Science Data*, *13*(11), 5151–5189. https://doi.org/10.5194/essd-13-5151-2021

Kumthekar, A., & Reddy, G. R. (2021). An integrated deep learning framework of U-Net and inception module for cloud detection of remote sensing images. *Arabian Journal of Geosciences*, *14*(18), 1900. https://doi.org/10.1007/s12517-021-08259-w

Kyzivat, E. D., Smith, L. C., Garcia-Tigreros, F., Huang, C., Wang, C., Langhorst, T., et al. (2022). The importance of Lake emergent aquatic vegetation for estimating Arctic-Boreal methane emissions. *Journal of Geophysical Research: Biogeosciences*, *127*(6), e2021JG006635. https://doi.org/10.1029/2021JG006635

Kyzivat, E. D., Smith, L. C., Pitcher, L. H., Fayne, J. V., Cooley, S. W., Cooper, M. G., et al. (2019). A high-resolution airborne color-infrared camera water mask for the NASA ABoVE campaign. *Remote Sensing*, *11*(18), 2163. https://doi.org/10.3390/rs11182163

McFeeters, S. K. (1996). The use of the normalized difference water index (NDWI) in the delineation of open water features. *International Journal of Remote Sensing*, *17*(7), 1425–1432. https://doi.org/10.1080/01431169608948714

Messager, M. L., Lehner, B., Grill, G., Nedeva, I., & Schmitt, O. (2016). Estimating the volume and age of water stored in global lakes using a geo-statistical approach. *Nature Communications*, *7*(1), 13603. https://doi.org/10.1038/ncomms13603

Mullen, A. (2023a). amullen01/dl-water-bodies: First_Release (Version v01). Zenodo. https://doi.org/10.5281/ZENODO.7689695

Mullen, A. (2023b). Model Files for Detecting Lakes and Ponds in PlanetScope Imagery with Deep Learning. Zenodo. https://doi.org/10.5281/ZENODO.7682754

Mullen, A., Watts, J. D., Rogers, B. M., Carroll, M. L., Caraballo-Vega, J. A., Noomah, J., et al. (2022). ABoVE: Lake and Pond Extent in Alaskan Boreal and Tundra Subregions, 2019-2021 (Version 1). ORNL Distributed Active Archive Center. https://doi.org/10.3334/ORNLDAAC/2134

Muster, S., Heim, B., Abnizova, A., & Boike, J. (2013). Water body distributions across scales: A remote sensing based comparison of three Arctic tundra wetlands. *Remote Sensing*, *5*(4), 1498–1523. https://doi.org/10.3390/rs5041498

Muster, S., Roth, K., Langer, M., Lange, S., Cresto Aleina, F., Bartsch, A., et al. (2017). PeRL: A circum-Arctic permafrost region pond and lake database. *Earth System Science Data*, *9*(1), 317–348. https://doi.org/10.5194/essd-9-317-2017

Negandhi, K., Laurion, I., Whiticar, M. J., Galand, P. E., Xu, X., & Lovejoy, C. (2013). Small thaw ponds: An unaccounted source of methane in the Canadian high Arctic. *PLoS One*, *8*(11), e78204. https://doi.org/10.1371/journal.pone.0078204

Nitze, I., Grosse, G., Jones, B. M., Romanovsky, V. E., & Boike, J. (2018). Remote sensing quantifies widespread abundance of permafrost region disturbances across the Arctic and Subarctic. *Nature Communications*, *9*(1), 5423. https://doi.org/10.1038/s41467-018-07663-3

NOAA National Centers for Environmental Information. (2021). Monthly national climate report for July 2021. Retrieved from https://www.ncei.noaa.gov/access/monitoring/monthly-report/national/202107

Pastick, N. J., Jorgenson, M. T., Wylie, B. K., Nield, S. J., Johnson, K. D., & Finley, A. O. (2015). Distribution of near-surface permafrost in Alaska: Estimates of present and future conditions. *Remote Sensing of Environment*, *168*, 301–315. https://doi.org/10.1016/j.rse.2015.07.019

Pekel, J.-F., Cottam, A., Gorelick, N., & Belward, A. S. (2016). High-resolution mapping of global surface water and its long-term changes. *Nature*, *540*(7633), 418–422. https://doi.org/10.1038/nature20584

Planet Team. (2021). Planet imagery product specifications.

Planet Team. (2022). UDM 2. Retrieved from https://developers.planet.com/docs/data/udm-2/

Qayyum, N., Ghuffar, S., Ahmad, H., Yousaf, A., & Shahid, I. (2020). Glacial lakes mapping using multi satellite PlanetScope imagery and deep learning. *ISPRS International Journal of Geo-Information*, *9*(10), 560. https://doi.org/10.3390/ijgi9100560

Rehder, Z., Zaplavnova, A., & Kutzbach, L. (2021). Identifying drivers behind spatial variability of methane concentrations in East Siberian ponds. *Frontiers of Earth Science*, *9*, 617662. https://doi.org/10.3389/feart.2021.617662

Rey, D. M., Walvoord, M., Minsley, B., Rover, J., & Singha, K. (2019). Investigating lake-area dynamics across a permafrost-thaw spectrum using airborne electromagnetic surveys and remote sensing time-series data in Yukon Flats, Alaska. *Environmental Research Letters*, *14*(2), 025001. https://doi.org/10.1088/1748-9326/aaf06f

Roy, D. P., Huang, H., Houborg, R., & Martins, V. S. (2021). A global analysis of the temporal availability of PlanetScope high spatial resolution multi-spectral imagery. *Remote Sensing of Environment*, *264*, 112586. https://doi.org/10.1016/j.rse.2021.112586

Seekell, D. A., & Pace, M. L. (2011). Does the Pareto distribution adequately describe the size-distribution of lakes? *Limnology & Oceanography*, *56*(1), 350–356. https://doi.org/10.4319/lo.2011.56.1.0350

Setiawan, A., Realino, B., Triyulianti, I., Hamzah, F., Murdimanto, A., Putri, M. R., & Nugroho, D. (2019). Using WorldView-2 imagery to estimate mangroves density in the porong estuary. In V. Barale & M. Gade (Eds.), *Remote sensing of the Asian Seas* (pp. 377–393). Springer International Publishing. https://doi.org/10.1007/978-3-319-94067-0_21

Sharma, R., Tateishi, R., Hara, K., & Nguyen, L. (2015). Developing superfine water index (SWI) for global water cover mapping using MODIS data. *Remote Sensing*, *7*(10), 13807–13841. https://doi.org/10.3390/rs71013807

Smith, L. C., Sheng, Y., MacDonald, G. M., & Hinzman, L. D. (2005). Disappearing Arctic lakes. *Science*, *308*(5727), 1429. https://doi.org/10.1126/science.1108142

Stanislawski, L. V., Shavers, E. J., Wang, S., Jiang, Z., Usery, E. L., Moak, E., et al. (2021). Extensibility of U-net neural network model for hydrographic feature extraction and implications for hydrologic modeling. *Remote Sensing*, *13*(12), 2368. https://doi.org/10.3390/rs13122368

Strayer, D. L., & Dudgeon, D. (2010). Freshwater biodiversity conservation: Recent progress and future challenges. *Journal of the North American Benthological Society*, *29*(1), 344–358. https://doi.org/10.1899/08-171.1

U.S. Geological Survey. (2020). *1 arc-second digital elevation models (DEMs)—USGS national map 3DEP downloadable data collection*. U.S. Geological Survey. Retrieved from https://nationalmap.gov/3DEP/

Verpoorter, C., Kutser, T., Seekell, D. A., & Tranvik, L. J. (2014). A global inventory of lakes based on high-resolution satellite imagery. *Geophysical Research Letters*, *41*(18), 6396–6402. https://doi.org/10.1002/2014GL060641

Villa, J. A., Ju, Y., Yazbeck, T., Waldo, S., Wrighton, K. C., & Bohrer, G. (2021). Ebullition dominates methane fluxes from the water surface across different ecohydrological patches in a temperate freshwater marsh at the end of the growing season. *Science of the Total Environment*, *767*, 144498. https://doi.org/10.1016/j.scitotenv.2020.144498

Walter Anthony, K., Schneider von Deimling, T., Nitze, I., Frolking, S., Emond, A., Daanen, R., et al. (2018). 21st-century modeled permafrost carbon emissions accelerated by abrupt thaw beneath lakes. *Nature Communications*, *9*(1), 3262. https://doi.org/10.1038/s41467-018-05738-9

Walter Anthony, K. M., Lindgren, P., Hanke, P., Engram, M., Anthony, P., Daanen, R. P., et al. (2021). Decadal-scale hotspot methane ebullition within lakes following abrupt permafrost thaw. *Environmental Research Letters*, *16*(3), 035010. https://doi.org/10.1088/1748-9326/abc848

Walvoord, M. A., Voss, C. I., & Wellman, T. P. (2012). Influence of permafrost distribution on groundwater flow in the context of climate-driven permafrost thaw: Example from Yukon Flats Basin, Alaska, United States: Permafrost distribution and groundwater flow. *Water Resources Research*, *48*(7), W07524. https://doi.org/10.1029/2011WR011595

Wangchuk, S., & Bolch, T. (2020). Mapping of glacial lakes using Sentinel-1 and Sentinel-2 data and a random forest classifier: Strengths and challenges. *Science of Remote Sensing*, *2*, 100008. https://doi.org/10.1016/j.srs.2020.100008

Watts, J. D., Kimball, J. S., Bartsch, A., & McDonald, K. C. (2014). Surface water inundation in the boreal-Arctic: Potential impacts on regional methane emissions. *Environmental Research Letters*, *9*(7), 075001. https://doi.org/10.1088/1748-9326/9/7/075001

Webb, E. E., Liljedahl, A. K., Cordeiro, J. A., Loranty, M. M., Witharana, C., & Lichstein, J. W. (2022). Permafrost thaw drives surface water decline across lake-rich regions of the Arctic. *Nature Climate Change*, *12*(9), 841–846. https://doi.org/10.1038/s41558-022-01455-w

Wik, M., Varner, R. K., Anthony, K. W., MacIntyre, S., & Bastviken, D. (2016). Climate-sensitive northern lakes and ponds are critical components of methane release. *Nature Geoscience*, *9*(2), 99–105. https://doi.org/10.1038/ngeo2578

Xu, N., Ma, Y., Wei, Z., Huang, C., Li, G., Zheng, H., & Wang, X. H. (2022). Satellite observed recent rising water levels of global lakes and reservoirs. *Environmental Research Letters*, *17*(7), 074013. https://doi.org/10.1088/1748-9326/ac78f8

References From the Supporting Information

Beven, K. J., & Kirkby, M. J. (1979). A physically based, variable contributing area model of basin hydrology/Un modèle à base physique de zone d'appel variable de l'hydrologie du bassin versant. *Hydrological Sciences Bulletin*, *24*(1), 43–69. https://doi.org/10.1080/02626667909491834

Chollet, F. (2015). Keras. Retrieved from https://keras.io

Cooley, S. W., Smith, L., Stepan, L., & Mascaro, J. (2017). Tracking dynamic northern surface water changes with high-frequency planet CubeSat imagery. *Remote Sensing*, *9*(12), 1306. https://doi.org/10.3390/rs9121306

Feng, W., Sui, H., Huang, W., Xu, C., & An, K. (2019). Water body extraction from very high-resolution remote sensing imagery using deep U-Net and a superpixel-based conditional random field model. *IEEE Geoscience and Remote Sensing Letters*, *16*(4), 618–622. https://doi.org/10.1109/LGRS.2018.2879492

Frazier, A. E., & Hemingway, B. L. (2021). A technical review of planet smallsat data: Practical considerations for processing and using PlanetScope imagery. *Remote Sensing*, *13*(19), 3930. https://doi.org/10.3390/rs13193930

Gillies, S. (2013). Rasterio: Geospatial raster I/O for Python programmers. *Mapbox*. Retrieved from https://github.com/rasterio/rasterio

Hasan, A., Udawalpola, M., Liljedahl, A., & Witharana, C. (2022). Use of commercial satellite imagery to monitor changing Arctic Polygonal Tundra. *Photogrammetric Engineering & Remote Sensing*, *88*(4), 255–262. https://doi.org/10.14358/PERS.21-00061R2

Huang, G., Liu, Z., van der Maaten, L., & Weinberger, K. Q. (2016). Densely connected convolutional networks (version 5). https://doi.org/10.48550/ARXIV.1608.06993

Joblove, G. H., & Greenberg, D. (1978). Color spaces for computer graphics. *ACM SIGGRAPH Computer Graphics*, *12*(3), 20–25. https://doi.org/10.1145/965139.807362

Jordahl, K., Bossche, J. V., Fleischmann, M., Wasserman, J., McBride, J., Gerard, J., et al. (2020). geopandas/geopandas: v0.8.1 (version v0.8.1). *Zenodo*. https://doi.org/10.5281/zenodo.3946761

Loesdau, M., Chabrier, S., & Gabillon, A. (2014). Hue and saturation in the RGB color space. In A. Elmoataz, O. Lezoray, F. Nouboud, & D. Mammass (Eds.), *Image and signal processing* (Vol. 8509, pp. 203–212). Springer International Publishing. https://doi.org/10.1007/978-3-319-07998-1_23

Olefeldt, D., Hovemyr, M., Kuhn, M. A., Bastviken, D., Bohn, T. J., Connolly, J., et al. (2021). The boreal–Arctic wetland and Lake Dataset (BAWLD). *Earth System Science Data*, *13*(11), 5127–5149. https://doi.org/10.5194/essd-13-5127-2021

Otsu, N. (1979). A threshold selection method from gray-level histograms. *IEEE Transactions on Systems, Man, and Cybernetics*, *9*(1), 62–66. https://doi.org/10.1109/TSMC.1979.4310076

Piliouras, A., & Rowland, J. C. (2020). Arctic river delta morphologic variability and implications for riverine fluxes to the coast. *Journal of Geophysical Research: Earth Surface*, *125*(1), e2019JF005250. https://doi.org/10.1029/2019JF005250

Porter, C., Morin, P., Howat, I., Noh, M.-J., Bates, B., Peterman, K., et al. (2018). ArcticDEM, version 3 [Dataset]. Harvard Dataverse. https://doi.org/10.7910/DVN/OHHUKH

Qin, P., Cai, Y., & Wang, X. (2022). Small waterbody extraction with improved U-Net Using Zhuhai-1 hyperspectral remote sensing images. *IEEE Geoscience and Remote Sensing Letters*, *19*, 1–5. https://doi.org/10.1109/LGRS.2020.3047918

qubvel. (n.d.). Segmentation Models. Retrieved from https://github.com/qubvel/segmentation_models

Ronneberger, O., Fischer, P., & Brox, T. (2015). U-Net: Convolutional networks for biomedical image segmentation. In N. Navab, J. Hornegger, W. M. Wells, & A. F. Frangi (Eds.), *Medical image computing and computer-assisted intervention—MICCAI 2015* (Vol. 9351, pp. 234–241). Springer International Publishing. https://doi.org/10.1007/978-3-319-24574-4_28

Rossum, G. V., & Drake, F. L. (2009). *Python 3 reference manual (version 3.9.1)*. Scotts Valley.

Sekertekin, A., Cicekli, S. Y., & Arslan, N. (2018). Index-based identification of surface water resources using Sentinel-2 satellite imagery. In *2018 2nd international symposium on multidisciplinary studies and innovative technologies (ISMSIT)* (pp. 1–5). IEEE. https://doi.org/10.1109/ISMSIT.2018.8567062

Tan, M., & Le, Q. V. (2020). EfficientNet: Rethinking model scaling for convolutional neural networks. arXiv. Retrieved from http://arxiv.org/abs/1905.11946

TensorFlow Developers. (2022). TensorFlow (version v2.8.2). *Zenodo*. https://doi.org/10.5281/ZENODO.4724125

Van der Walt, S., Schönberger, J. L., Nunez-Iglesias, J., Boulogne, F., Warner, J. D., Yager, N., et al. (2014). scikit-image: Image processing in Python. *PeerJ*, *2*, e453. https://doi.org/10.7717/peerj.453

Wang, J., Yang, D., Chen, S., Zhu, X., Wu, S., Bogonovich, M., et al. (2021). Automatic cloud and cloud shadow detection in tropical areas for PlanetScope satellite images. *Remote Sensing of Environment*, *264*, 112604. https://doi.org/10.1016/j.rse.2021.112604

Xu, H. (2006). Modification of normalized difference water index (NDWI) to enhance open water features in remotely sensed imagery. *International Journal of Remote Sensing*, *27*(14), 3025–3033. https://doi.org/10.1080/01431160600589179